

Article

Hybrid Locomotion Evaluation for a Novel Amphibious Spherical Robot

Huiming Xing ¹ , Shuxiang Guo ^{1,2,*}, Liwei Shi ^{1,*} , Yanlin He ¹, Shuxiang Su ¹, Zhan Chen ¹ and Xihuan Hou ¹

¹ Key Laboratory of Convergence Medical Engineering System and Healthcare Technology, the Ministry of Industry and Information Technology, School of Life Science, Beijing Institute of Technology, Beijing 100081, China; xinghuiming@bit.edu.cn (H.X.); heyanylin@bit.edu.cn (Y.H.); sushuxiang@bit.edu.cn (S.S.); chenzhan@bit.edu.cn (Z.C.); houxihuan@bit.edu.cn (X.H.)

² Faculty of Engineering, Kagawa University, 2217-20 Hayashicho, Takamatsu, Kagawa 761-0396, Japan

* Correspondence: guoshuxiang@bit.edu.cn (S.G.); shiliwei@bit.edu.cn (L.S.); Tel.: +86-159-1102-2732 (S.G.); +86-10-6891-5908 (L.S.)

Received: 14 November 2017; Accepted: 10 January 2018; Published: 24 January 2018

Abstract: We describe the novel, multiply gaited, vectored water-jet, hybrid locomotion-capable, amphibious spherical robot III (termed ASR-III) featuring a wheel-legged, water-jet composite driving system incorporating a lifting and supporting wheel mechanism (LSWM) and mechanical legs with a water-jet thruster. The LSWM allows the ASR-III to support the body and slide flexibly on smooth (flat) terrain. The composite driving system facilitates two on-land locomotion modes (sliding and walking) and underwater locomotion mode with vectored thrusters, improving adaptability to the amphibious environment. Sliding locomotion improves the stability and maneuverability of ASR-III on smooth flat terrain, whereas walking locomotion allows ASR-III to conquer rough terrain. We used both forward and reverse kinematic models to evaluate the walking and sliding gait efficiency. The robot can also realize underwater locomotion with four vectored water-jet thrusters, and is capable of forward motion, heading angle control and depth control. We evaluated LSWM efficiency and the sliding velocities associated with varying extensions of the LSWM. To explore gait stability and mobility, we performed on-land experiments on smooth flat terrain to define the optimal stride length and frequency. We also evaluated the efficacy of waypoint tracking when the sliding gait was employed, using a closed-loop proportional-integral-derivative (PID) control mechanism. Moreover, experiments of forward locomotion, heading angle control and depth control were conducted to verify the underwater performance of ASR-III. Comparison of the previous robot and ASR-III demonstrated the ASR-III had better amphibious motion performance.

Keywords: the amphibious spherical robot; the lifting and supporting wheel mechanism; sliding locomotion; wheel-legged robot; waypoints tracking; hybrid locomotion

1. Introduction

Amphibious robots are currently under development. Such robots can both walk on rough terrain and swim, and are reliable, stable, able to work rapidly and carry large loads, and display intelligence. These robots have been widely and successfully used for monitoring, recovery, detection of pollution, submarine sampling, data collection, video-mapping, vision perception [1], exploration of unstructured amphibious environments, object recovery under challenging circumstances, and other tasks [2–5].

Recently, many robotic designs [6–8] have been inspired by biology, especially amphibious robots differing in terms of propulsion method and shape. Inspired by the crab and the lobster, Jun et al.

developed a multi-legged underwater-walking robot (CR200) [9,10] to survey underwater structures and shipwrecks off the coast of the Korean Peninsula; the robot is slow because it features legged propulsion. In 2013, Crespi designed a bio-amphibious salamander robot (*Salamandra robotica II*) [11] that both walked and swam; the robot has four legs and an active spine allowing anguilliform swimming in water and on-ground walking with various gaits, featuring body-limb coordination and bodily undulation. Earlier, in 2006, Crespi et al. created an amphibious snake robot termed *AmphiBot II* [12] that crawled and swam using a central-pattern generator. In 2009, Tang developed a wheel-propeller-leg-integrated amphibious robot [13] that crawled on land, swam underwater (at certain depths), and crept on the ocean floor. In 2016, Zhang developed the amphibious robot *AmphiHex-I* [14] which walked on rough terrain, maneuvered underwater, and used specially designed transformable flipper legs to traverse soft muddy or sandy substrates in littoral areas between land and water. All of these amphibious robots have particular characteristics and advantages. In terms of on-land locomotion, legged robots [15–18] deal better with uneven terrain, but are slow, whereas wheeled robots [19,20] move rapidly but cope poorly with rough ground; serpentine robots [21,22] (inspired by snakes) work well on flat terrain but it is difficult to control the direction and speed of motion. In water, robots with screw propellers are more stable and mobile than those with oscillatory and undulatory capacities.

Earlier, inspired by amphibious turtles, the amphibious spherical robot I (ASR-I) [23,24] that could move both on land and underwater was constructed. The ASR-I diameter (including its four legs) was only 25 cm. To improve stability while retaining precision, we built the ASR-II [25–28] using 3-D printing. This robot could walk at up to 8.5 cm/s (0.34 the body length) and climb a slope of 5°. To improve locomotion on land, Li added a propulsion mechanism featuring active wheels [29]. The direct current (DC) motors driving the wheels increased the speed. An active wheel-legged robot [30] with 6 legs was developed to get better actions in unknown environment with reinforcement learning. The robot used values of external force measured on the robot's legs as states and rewards, and it can adapt to different terrains in real time using on-line learning. However, propulsion system redundancy was evident, and the active wheels (with DC motors) increased the size of the robot, causing problems during walking.

The passive wheel-legged robot named *Roller-walker* [31–34] with two locomotion modes was early proposed. *Roller-walker* can transform into sole mode by rotating the ankle roll joint with the passive wheel on each leg. Using the transformation mechanism, the robot can switch between the quadruped walking and roller-skating on smooth flat terrain. The transformation of the actuation modes can be realized by one degree of freedom of each leg. The mechanical legs were redesigned to feature four passive wheels [35], allowing the amphibious robot to move rapidly on smooth flat ground. The robot exhibited both roller-skating and walking locomotion. Compared with active-wheeled robots, passive wheel-legged robots are of lower weight, consume less energy, and are smaller. However, directional control of passive wheel-legged robots is difficult; such robots swing while walking and skating.

Therefore, to enhance the space available for sensors, and to improve on-land stability and velocity, we developed a sliding mode-based, amphibious spherical robot employing a wheel-legged, water-jet, composite driving mechanism (including a lifting and supporting wheel mechanism (LSWM)) and mechanical legs with water-jet thruster. To allow the robot to readily move in any direction, four omni-directional passive wheels were added to the LSWM mobile platform. The LSWM lifts and drops the mobile platform. The robot undergoes sliding locomotion when the platform is lowered, and walking locomotion when the platform is raised. Therefore, the robot combines the advantages of locomotion afforded by legs and wheels when walking on rough terrain, and sliding locomotion on flat ground or slopes. We conducted a waypoint tracking experiment using a vision localization system to evaluate stability, velocity, and directional control. Finally, the underwater locomotion experiments with four vectored water-jet thrusters was conducted to evaluate the performance of underwater locomotion.

The remainder of this paper is organized as follows: In Section 2, we describe our advanced design of such a robot, the wheel-legged water-jet composite driving mechanism, the new LSWM assisting the robot to stand or slide, and the electrical system delivering either strong or weak power. Section 3 presents the forward and inverse kinematic models of the mechanical legs, the novel sliding and walking locomotors gait based on the LSWM, the underwater locomotion. In Section 4, we describe experiments verifying the LSWM, the sliding and walking gaits using the LSWM, and the comparison of two on-land locomotion on different terrain. A waypoint tracking experiment evaluates the reliability and feasibility of the robot in real work using a closed-loop proportional-integral-derivative (PID) control mechanism. We conducted forward motion experiment and heading angle control experiment in Section 5. Sections 6 and 7 conclude the paper.

2. The Amphibious Spherical Robot (ASR) III

2.1. The Mechanism

To create more space for sensors, and to improve stability and velocity on land, we designed an on-land, multiple-locomotion-based, amphibious spherical robot. As shown in Figure 1, the robot has a hemispherical waterproof hull, two quarter-spherical hulls, a central plant, four mechanical legs, a mechanism for lifting and supporting the wheels, an electrical circuit, and five batteries. The thickness of the hemispherical hull, which is made of Acrylonitrile Butadiene Styrene (ABS) plastic, is about 6 mm, adequate to allow the robot to operate up to 10 m underwater. The top of the hull has a waterproof plug; when this is removed, the control system of the robot can be connected to a remote computer via an optical fiber cable, allowing software debugging. An O-ring is placed between the hemispherical hull and the central plant to ensure waterproofing; again, the manual indicates that the robot can dive to a maximum of 10 m. The actuator is a wheel-legged composite mechanism including the LSWM and mechanical legs. In the water, the two quarter-spherical hulls close up like a ball and the robot moves using four vectored water-jet thrusters. On land, the two hulls open and the robot can slide or walk using the wheel-legged composite driving mechanism. To deal with the extra weight, five batteries, one of which contains 6000 mAh, are used to extend the working time.

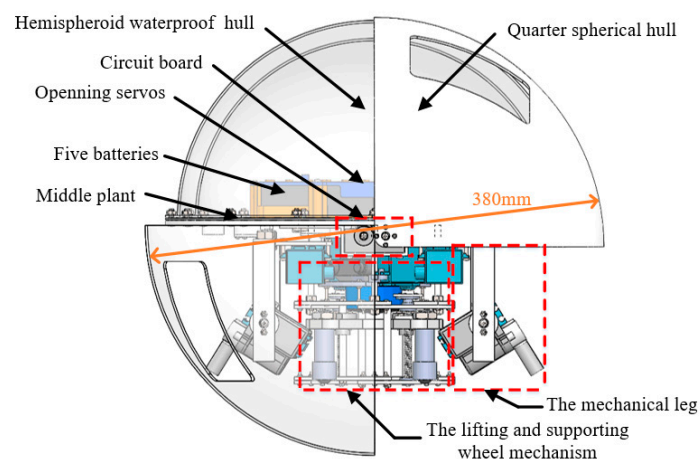


Figure 1. The novel amphibious spherical robot III (ASR-III).

2.2. The Wheel Legged Water-Jet Composite Driving Mechanism

As more multifunctional sensors are required when a robot increases in size and weight, the actuation mechanism becomes challenging. The robot diameter was 35 cm following a redesign to include more sensors. Buoyancy calculations indicated that the weight needed to be 11.22 kg before the robot sank in water. When standing, the four mechanical legs must support the robot and the numerous sensors; there is a danger that a sudden current surge might burn out the electronic

circuit. Thus, we developed a wheel-legged and water-jet composite driving mechanism including the LSWM (Figure 2a) and mechanical legs (Figure 2b). The LSWM assists the robot to stand and perform on-land locomotion that is rapid on smooth, flat terrain. The mechanism reduces wear on the actuating mechanism (the steering gear, etc.), extending the working life of the robot. Also, the robot can slide down slopes, which saves a great deal of power.

The LSWM is shown in Figure 2a. At the top, two servos can rotate through 360 degrees. The mechanism includes an upper support platform with four top beams and a lower support platform with four lower beams. A mobile platform with four supporting legs allows automatic transition between the sliding and walking modes. The ends of the legs bear four omni-directional wheels, allowing the robot to slide in any direction on flat, smooth terrain. As shown in Figure 2b, the mechanism also includes a mechanical leg with two joints, two servos, two omni-directional wheels, an upper holder, a lower holder, and a water-jet thruster. In previous work [36], the thruster was just used to spray water in one direction. Now, by the LM298N, a motor driving module, the thruster can spray the water in two directions. Therefore, for the forward motion and rotary motion in water, four water-jet thrusters all can be used simultaneously. The details are described in Section 3.

When the robot moves from rough to smooth terrain, the two servos rotate in the same direction, simultaneously and synchronously, and the mobile platform drops vertically along the guide bar. Then, using the four mechanical legs, the robot switches to sliding locomotion. When the robot walks on rough terrain, the two servos rotate in the opposite direction simultaneously and synchronously, lifting the mobile vertically.

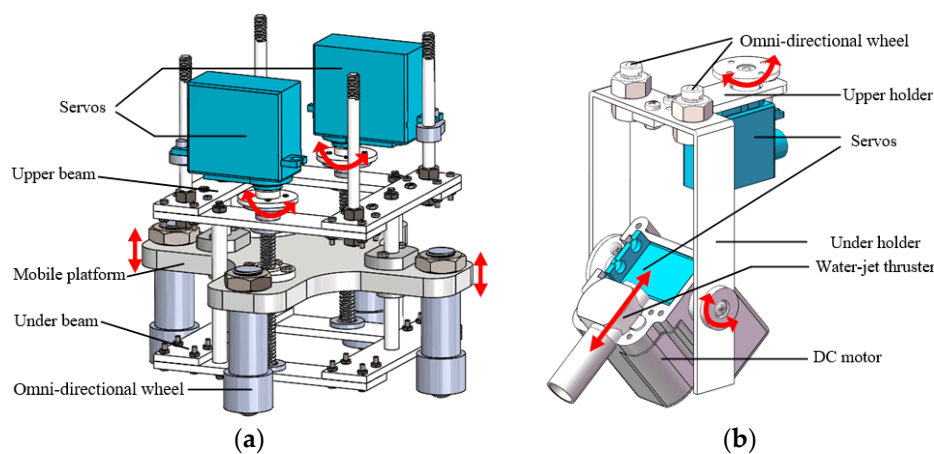


Figure 2. The wheel-legged, water-jet composite driving mechanism. (a) The lifting and supporting wheel mechanism; (b) The mechanical leg of ASR-III.

The frequency of the control signal is 50 Hz, and the duty factor S_{PWM} of the pulse width modulation (PWM) signal can be set to obtain the desired angular velocity w ; the relationship is described by Equation (1).

$$w = kS_{PWM} \tag{1}$$

where, k is the scaling factor between the angular velocity and the duty factor of PWM signal.

The LSWM is modeled using Equation (2).

$$H = \Delta l \times \frac{n \times 2\pi}{kS_{PWM}} \tag{2}$$

where H is the distance through which the support platform travels, Δl is the length travelled as the servo rotates once, n is the number of rotations, S_{PWM} is the PWM signal value, and k is as described above.

2.3. The Electrical Circuit

To improve the stability and logic of the circuit (Figure 3), we divided it into four parts: the power supply unit (PSU), the decision center, and sensor and driver layers. A stable, powerful, electrically isolated PSU is essential. When the robot begins to stand, eight servos require electricity simultaneously, triggering a surge current that challenges the controller and sensors. Hence, we used five 8.4-V batteries, two of which (Battery II) power the decision center and the sensor layer, and three of which (Battery I) power the controls and the driver layer. To isolate the control and dynamic electricity, they are not common-grounded; the control system outputs PWM signals to the motors of the dynamic system via optocouplers that transform photoelectric signals. We used a Zynq-7000 SoC system as the “brain”, to offer a platform which has the computational capabilities to realize the intelligence and function of the robot. When exploring and sensing amphibiously, the robot uses many sensors, such as a Global Positioning System (GPS), an inertial navigation system (INS), cameras, pressure sensors, and a communication modem; all signals are sent to the decision center. In this paper, the JY901 IMU module with high-precision is a key sensor giving the angle feedback for motion control, and installed in the center of the PCB board. IIC bus is used to produce data and make it available to the Zynq-7000 SoC system.

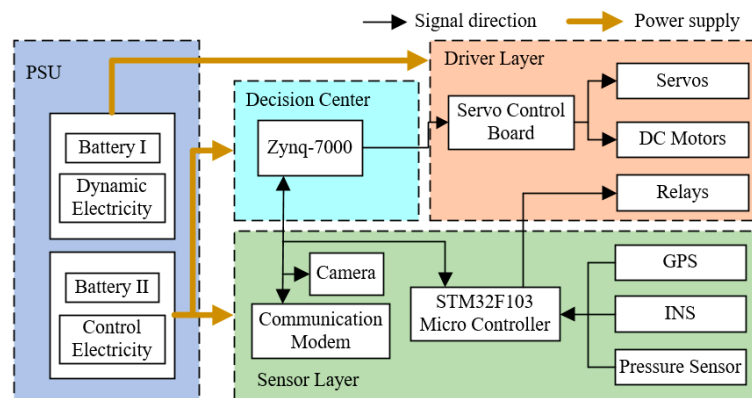


Figure 3. The circuit system of ASR-III. DC: direct current; GPS: Global Positioning System; INS: inertial navigation system.

3. The Hybrid Locomotion

A multiply gaited, vectored water-jet, hybrid locomotion was designed for ASR-III to improve the performance in amphibious environment. Different gaits on land afford distinct advantages in terms of speed, stability and energy consumption; specific substrates require different gaits. For example, walking on mechanical legs with multiple degrees of freedom is optimal on rough terrain. However, on smooth flat terrain and slopes, sliding locomotion for ASR-III is much better in terms of velocity, energy efficiency and stability. Besides on-land locomotion, underwater locomotion is actuated by four vectored water-jet thrusters, and the robot is capable of forward motion, heading angle control, and depth control. Therefore, a multi-locomotion capacity greatly improves robotic performance and practicability in amphibious environment.

3.1. Forward Kinematic Model of ASR-III

To describe the locomotion of the leg-wheeled robot simply, we term the four legs LF, LH, RH, and RF (the left foreleg, left hind leg, right hind leg, and right foreleg, respectively; Figure 4). The Figure 4 shows the coordinate system $\{O_B\}$ of the trunk and assumes that the coordinate lies in the geometrical center of the trunk. The X_B axis represents the forward direction, the Z_B axis the vertical direction (perpendicular to the trunk’s horizontal plane), and the Y_B axis the direction to the right of the trunk. Figure 4 shows the coordinates of the legs $\{O_0^i\}$ where i represents a leg number ($i = 1$ for LF, $i = 2$

for LH, $i = 3$ for RH, and $i = 4$ for RF). The coordinates of each leg are similar; we describe only the coordinates of the left foreleg in Figure 5. Each leg has a hip joint, a knee joint, and a toe, corresponding to the coordinates $\{O_1\}$, $\{O_2\}$, and $\{O_3\}$, respectively.

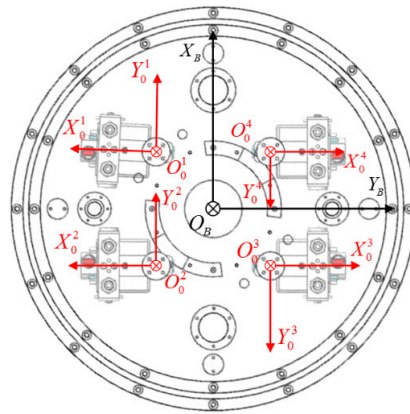


Figure 4. The coordinates of the robot and the legs (top view).

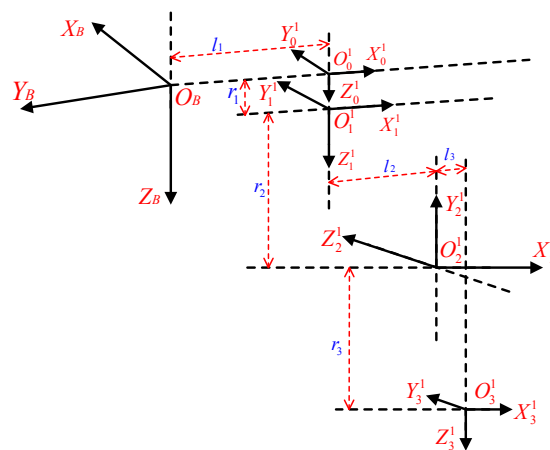


Figure 5. Kinematics model of the left foreleg of ASR-III.

For on-land locomotion of the leg-wheeled robot, it can be known that two parameters (the stride and frequency) influence the velocity of the robot. In order to get a high velocity, the stride length and frequency need to be increased. Considering the compact structure of ASR-III, the design using servo motors is a nice choice to the mechanical leg. Every leg has two degrees of freedom with two servo motors. The bottom and center of the middle plant is a good site to install the communication module. In order to hold the communication module and lower the barycenter of the robot, the height of the LSWM was decided to 12.1 cm. As shown in Figure 2a, the distance from the upper state to the lower state was 2.5 cm. With the increasing of the under holder, the robot gets a higher barycenter, which decreases the stability of ASR-III. Therefore, to obtain a lower barycenter and make the robot stand up at the lower state of LSWM, the length of the under holder shown in Figure 2b was decided to 9.5 cm. In our robot, the longer the upper holder, the longer the stride length. However, for keeping the spherical boundary, the longest length of the upper holder was 4 cm. The robot was designed using Solidworks 2017. In addition, avoiding interference of parts in assembly, all the parameters of the leg were optimized to get a higher velocity of sliding locomotion and walking locomotion, and a lower barycenter for ASR-III.

Table 1 lists all of the Denavit-Hartenberg (D-H) parameters of the left foreleg. θ_j^i and d_j^i are the joint angle and the distance between the joint $j - 1$ and j of leg i ; and α_{j-1}^i and a_{j-1}^i are the torsional

angle and the length of the bar $j - 1$ of leg i , respectively. The five principal physical parameters of the leg are shown in Table 1. The parameter l_1 , the horizontal distance from the center of the plant to the hip joint, is 70 mm.

Table 1. The Denavit-Hartenberg (D-H) parameters of the left foreleg.

Joint j	α_j^i	\mathbf{ff}_{j-1}^i	\mathbf{ff}_{j-1}^i (mm)	d_j^i (mm)	α_j^i
1	$\theta_1^1(0)$	0	0	$r_1(10)$	$(0, \pi/2)$
2	$\theta_2^1(0)$	0	$l_2(40)$	$r_2(95)$	$(-\pi/6, \pi/4)$
3	0	$\pi/2$	$l_3(20)$	$r_3(60)$	0

Using the D-H homogeneous transformation formula in the driven-axis context, we obtain Equation (3).

$${}^B\mathbf{T}_3^1 = \begin{bmatrix} s_1^1 c_2^1 & c_1^1 & s_1^1 s_2^1 & l_3 s_1^1 c_2^1 + r_3 s_1^1 s_2^1 + l_2 s_1^1 + l_1 \\ -c_1^1 c_2^1 & s_1^1 & -c_1^1 s_2^1 & -l_3 c_1^1 c_2^1 - r_3 c_1^1 s_2^1 - l_2 c_1^1 - l_1 \\ -s_2^1 & 0 & c_2^1 & -l_3 s_2^1 + r_3 c_2^1 + r_3 + r_1 \\ 0 & 0 & 0 & 1 \end{bmatrix} \tag{3}$$

where, $s_j^i = \sin \theta_j^i$ and $c_j^i = \cos \theta_j^i$.

The position of the toe of the left foreleg in terms of the trunk coordinates can be obtained as follows Equation (4).

$$\mathbf{p}^1 = \begin{bmatrix} p_x^1 \\ p_y^1 \\ p_z^1 \end{bmatrix} = \begin{bmatrix} l_3 s_1^1 c_2^1 + r_3 s_1^1 s_2^1 + l_2 s_1^1 + l_1 \\ -l_3 c_1^1 c_2^1 - r_3 c_1^1 s_2^1 - l_2 c_1^1 - l_1 \\ -l_3 s_2^1 + r_3 c_2^1 + r_3 + r_1 \end{bmatrix} \tag{4}$$

Similarly, the equations of the left hind leg, the right hind leg and the right foreleg also can be obtained by the same procedure of the left front leg. The forward kinematic model can be succinctly written as Equation (5).

$${}^B\mathbf{p}_{toe} = FK(\theta) \tag{5}$$

where, FK represents the inverse kinematics, allowing mapping from the joint space to the Cartesian space.

3.2. Inverse Kinematic Model

The movement required to control the robot can be calculated using the inverse kinematic model. We derive inverse kinematic equations employing the forward kinematic model.

When the left forward toe is in position $\mathbf{p}_{toe}^1 = [p_x^1 \ p_y^1 \ p_z^1]^T$ of $\{O_B\}$, its position in other coordinate systems can be obtained by inverse transformation. The position in $\{O_1\}$ is expressed by Equation (6).

$${}^1\mathbf{T}_3^1 = ({}^0\mathbf{T}_1^1)^{-1} ({}^B\mathbf{T}_0^1)^{-1} {}^B\mathbf{T}_3^1 = \begin{bmatrix} c_1^1 n_x^1 + s_1^1 n_y^1 & c_1^1 o_x^1 + s_1^1 o_y^1 & c_1^1 a_x^1 + s_1^1 a_y^1 & s_1^1 (p_x^1 - l_1) - c_1^1 (p_y^1 + l_1) \\ -s_1^1 n_x^1 + c_1^1 n_y^1 & -s_1^1 o_x^1 + c_1^1 o_y^1 & -s_1^1 a_x^1 + c_1^1 a_y^1 & c_1^1 (p_x^1 - l_1) + s_1^1 (p_y^1 + l_1) \\ n_z^1 & o_z^1 & a_z^1 & p_z^1 - r_1 \\ 0 & 0 & 0 & 1 \end{bmatrix} \tag{6}$$

Then, the position also can be obtained as Equation (7).

$${}^1\mathbf{T}_3^1 = {}^1\mathbf{T}_2^1 {}^2\mathbf{T}_3^1 = \begin{bmatrix} c_2^1 & 0 & -s_2^1 & l_3 c_2^1 + r_3 s_2^1 + l_2 \\ 0 & -1 & 0 & 0 \\ -s_2^1 & 0 & -c_2^1 & -l_3 s_2^1 + r_3 c_2^1 + r_2 \\ 0 & 0 & 0 & 1 \end{bmatrix} \tag{7}$$

Employing Equations (6) and (7), we obtain Equation (8) containing two joint variables,

$$\begin{cases} s_1^1(p_y^1 + l_1) + c_1^1(p_x^1 - l_1) = 0 \\ -l_3s_2^1 + r_3c_2^1 + r_2 = p_z^1 - r_1 \end{cases} \quad (8)$$

Define $t = p_z^1 - r_2 - r_1$. Then, we obtain Equation (9).

$$\begin{cases} \theta_1^1 = \text{atan2}(l_1 - p_x^1, l_1 + p_y^1) \\ \theta_2^1 = \text{atan2}(r_3, l_3) - \text{atan2}(t, \pm\sqrt{r_3^2 + l_3^2 - t^2}) \end{cases} \quad (9)$$

Similarly, the equations of the left hind leg, the right hind leg and the right foreleg also can be obtained by the same procedure. The inverse kinematic model can be succinctly written as Equation (10).

$$\theta = IK({}^B p_{toe}) \quad (10)$$

where IK refers to the inverse kinematics, allowing mapping from the Cartesian space to the joint space.

3.3. Multiple On-Land Locomotion

Our earlier robot had a diameter of 20 cm and used four legs for support. The new robot is 35 cm in diameter (enlarged to carry more sensors), rendering it much heavier. It is challenging to support the body with four mechanical legs. Therefore, we designed the LSWM to allow the robot to slide on land like a turtle. We carefully observed how a turtle moved, and used this principle to design the gaits. To move flexibly and steadily, the turtle uses both symmetrical and asymmetrical gaits. The symmetrical gait is basically a trot (a two-beat gait) (Figure 6b) and the asymmetrical gait is basically a tripod walk (a four-beat gait) (Figure 6a); the synchronous gaits are shown in Figure 6c–e. When trotting, the four legs move in the sequence “LH, RF → LF, RH → LH, RF”, as shown in Figure 7b. We set the duty factors during the transfer phase to 50%. The sequence of the tripod walk shown in Figure 7a is “LF → RH → RF → LH”, and the duty factor is about 75%. During synchronous sliding with two legs (Figure 7c), the sequence is “LF, RF → LF, LH”, and the duty factor is 50%. The turtle also performs synchronous sliding using four legs, as shown in Figure 6d, to achieve both forward and rotatory locomotion. In the real world, turtles often move from one point to another. When moving short distances using little energy, the turtle rotates with a zero radius if it wants to go back. Therefore, we implemented a rotary gait with zero radius as the directional control; the duty factor was 50%. Thus, like the turtle, the robot can turn left and right.

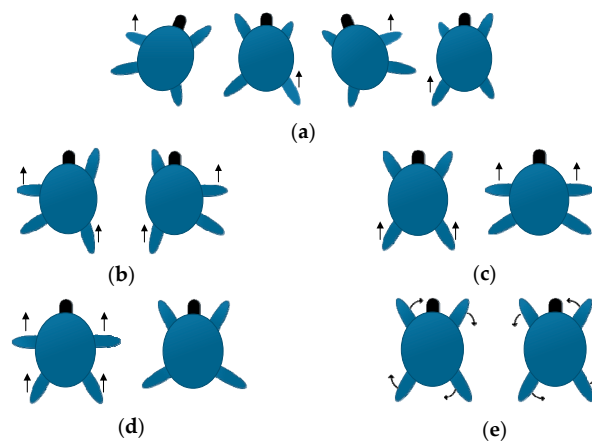


Figure 6. Turtle gaits (The black arrow indicates that the leg is in transfer phase). (a) The tripod walking gait (TPWG); (b) the trotting walking gait (TTWG); (c) the synchronous sliding gait with two legs (SSGTL); (d) the synchronous sliding gait with four legs; (e) the rotary sliding gait with zero radius.

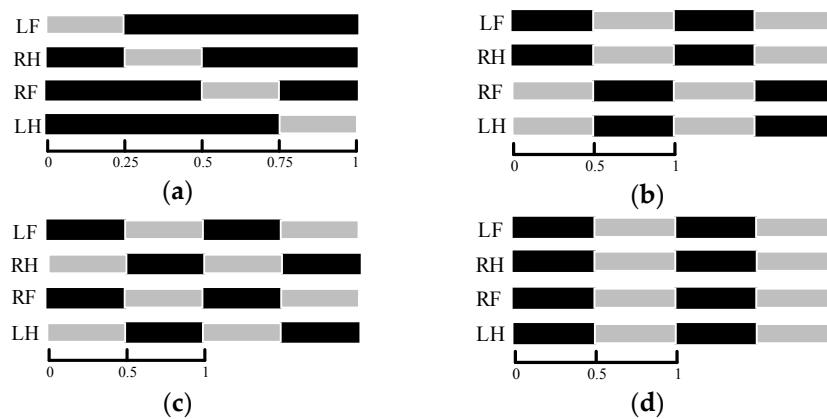


Figure 7. The sequence of the gaits. (a) TPWG; (b) TTWG; (c) SSGTL; (d) the synchronous sliding gait with four legs. The gray and the black bars show that the leg is in the transfer and support phase, respectively. Over single cycles of the trotting and synchronous gaits, the robot simultaneously has two legs in the transfer phase and two legs in the support phase. When in the synchronous sliding gait, the four legs of the robot swing synchronously with the same stride, generating different types of locomotion (rotatory or forward, based on different leg swing directions). Over a single cycle of TPWG, only one leg is in the transfer phase and, under the same conditions, the cycle time is twice that of the other three synchronous gaits.

3.4. Underwater Locomotion

Every water-jet thruster of four legs can rotate in the vertical and horizontal planes. With the directions and propulsive forces of four vectored water-jet thrusters changing, the robot can move forward or backward, turn left or right, float or sink in the underwater environment. Figure 8 illustrates the underwater locomotion of the robot.

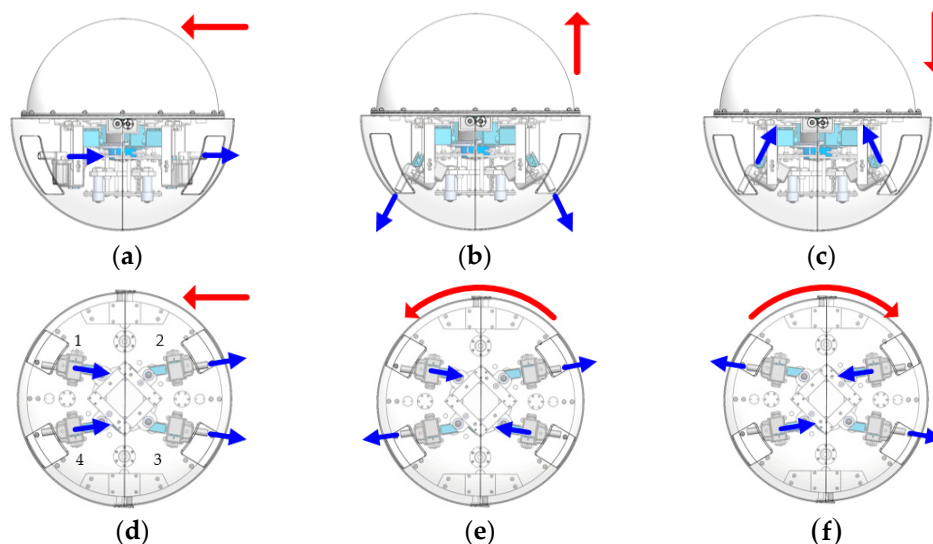


Figure 8. Underwater locomotion. Side view: (a) forward motion; (b) floating motion; (c) sinking motion. Bottom view: (d) forward motion; (e) left turning motion; (f) right turning motion. The blue arrow indicates the water-jet direction of the thruster, and the red arrow represents the motion direction of the robot.

The four legs are denoted by number 1, 2, 3 and 4, as shown in Figure 8d. Leg 1 and 2 are on the left of the robot, and leg 3 and 4 on the right. As depicted in Figure 8a,d, the robot can adjust the water-jet direction of thrusters in the same horizontal plane to realize forward or backward motion.

In addition, by the difference of the left water-jet force and the right water-jet force, the robot can implement the left and right turning motion, as shown in Figure 8e,f. Besides, as shown in Figure 8b,c, with adjusting the direction and force of four water-jet thrusters in the vertical plane, the robot can float upward and sink down. With the flexible motion, our robot can be used for environment monitoring, object tracking and detection of pollution with proper sensors.

4. The On-Land Locomotion Experiments

We performed experiments to verify the reliability and feasibility of the LSWM, an essential feature of sliding locomotion. We measured the distance that the LSWM traveled, and acquired the optimal length and frequency of the stride for the sliding and walking locomotion modes on different terrain.

4.1. The Lifting and Supporting Wheel Mechanism (LSWM)

To reduce the load on the actuator and extend its working life, we developed an LSWM driven by two 360-degree servos. Before the robot moved, the mobile platform descended, powered by the two servos rotating synchronously in the same direction. The PWM control signals were sent to the servos by the motor control board. We used waterproof servos (model HDKJ D3009) with a working voltage of 4.8–7.2 V. To maximize force and torque, we selected 7.2 V as the working voltage. The stall torque was 10 kg·cm and the operating speed was 0.14 s/60°. The frequency of the control signal was 50 Hz, and the duty factor s of the PWM signal ranged from 6.9 to 8.1%. We set the step size of the PWM signal to 0.05%. Thus, we obtained 20 data groups (from the lower to the upper and from the upper to the lower states, as shown in Figure 9); the distance Δh between the upper and lower state was 40 mm. All data groups were collected 10 times and averaged. The rising and falling velocities were as Equation (11).

$$v = \frac{\Delta h}{t} \quad (11)$$



Figure 9. (a) The upper state of lifting and supporting wheel mechanism (LSWM); (b) the lower state of LSWM.

The nonlinear relationship between the rising and falling velocity v and the duty factor s is shown in Figure 10. We considered the falling velocity positive and the rising velocity negative. When the duty factor ranged between 7.41 and 7.51%, the servo torque was very low and the LSWM velocity was almost zero. When the duty factor was more than 7.9% or less than 7.05%, the servo angular velocity, rendering both the rising and falling velocity relatively stable. Finally, based on the variation in velocity as the duty factor ranged from 7 to 8%, the nonlinear relationship can be described by the sum of sines (Equation (12)).

$$v = \begin{cases} -2.1 & s < 7.1 \\ 0 & 7.41 < s < 7.51 \\ 2.1 & s > 7.9 \\ 1.968 \sin(3.448s + 18.22) + 0.1923 \sin(9.059s + 23.33) & \textit{else} \end{cases} \quad (12)$$

When the robot moves from flat, smooth terrain to rough terrain and vice versa, autonomous stable transition from sliding to walking (or vice versa) is achieved by varying the duty factor, dramatically improving performance on different substrates.

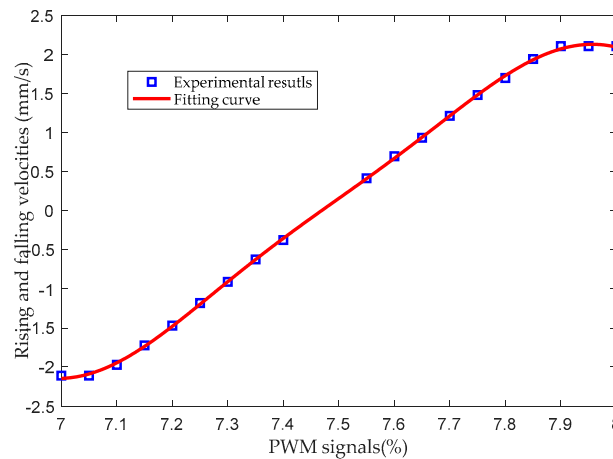


Figure 10. The relationship between the duty factor and the velocity. The falling velocity is positive, and the rising velocity negative.

4.2. Sliding Locomotion Using the LSWM

Sliding is appropriate on smooth flat terrain. Below a certain frequency, the velocity of the sliding gait varies with the distance by which the LSWM falls. As the mobile platform descends, the toe can touch the ground with the knee joint rotated clockwise, reducing the horizontal distance Δl from the knee joint to the toe. As shown in Figure 11, the blue state ($\Delta h = 11$ mm) of the leg reflects the situation where the toe only just touches the ground, and the red state ($\Delta h = 36$ mm) reflects the situation when the stance is vertical. Therefore, the fall distance Δh is 11–36 mm. We used HS-5646 WP servos, rotating at a rate of 0.18 s/ 60° at 7.4 V. We set the rotary angle θ_1^i and the rotary speed w_s of the horizontal servo to 90° and 0.5 s/ 60° respectively, in case a slice developed. We obtained the velocity of the sliding gait by Equations (13) and (14).

$$v = \frac{l}{t} = \frac{l_2 + \Delta l}{t} = \frac{l_2 + \sqrt{R^2 - [r_3 - (36 - \Delta h)]^2}}{t} \quad (13)$$

$$t = 2\theta_1^i w_s \quad (14)$$

where R is the distance from the knee joint to the toe ($R = 63.25$ mm).

To evaluate sliding locomotion using the LSWM on smooth flat ground, we modeled a synchronous sliding gait using two legs. We measured the sliding velocities at different descent values Δh of the mobile platform. In Figure 12, the blue curve shows a simulation of sliding velocity based on Equations (13) and (14). The deep-sky-blue circles indicate the experimental sliding velocities. We set 1 mm as the step size, and obtained 25 groups of experimental results from 11 to 36 mm. The maximum velocity was 10.2 cm/s at $\theta_2^i = 37.97^\circ$ and $\Delta h = 11$ mm. As the descent distance of the mobile platform increased, the velocity declined to 66.5 mm/s. The experimental and simulated results

differed by about 10 mm, which may reflect installation error. However, the trends of the two curves were similar.

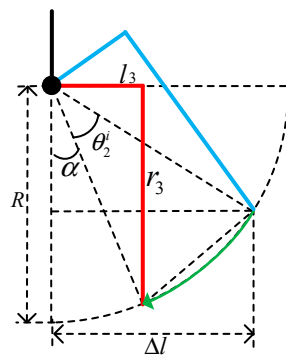


Figure 11. Extent of rotation of the knee joint by LSWM descent distance. The blue state ($\Delta h = 11$ mm) indicates that the toe only just touches the ground, and the red state ($\Delta h = 36$ mm) indicates the vertical stance. The green arrow indicates that the knee joint rotates from the blue to the red state.

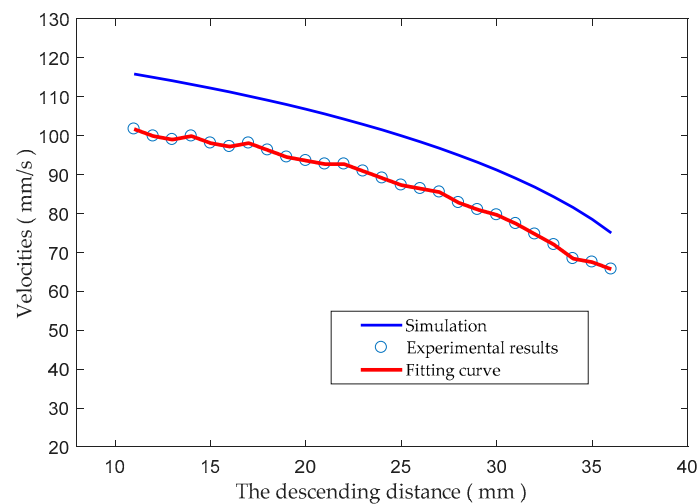


Figure 12. The sliding velocities at different descent distances.

4.3. Two On-Land Locomotion Experiments

To measure sliding mode velocities, we evaluated the relationships between robot velocity, and the swing frequency and angle of the legs. For sliding locomotion and walking locomotion of ASR-III, two key parameters affecting velocity are the stride length and frequency. To evaluate performance on land, we conducted sliding and walking experiments exploring these parameters.

When walking, the velocity is given by Equation (15).

$$v = s_L \times f \tag{15}$$

where, s_L is the length of one stride in the x direction, and f is the stride frequency. Using the ASR-III kinematic model, the stride in the x direction is given by Equation (16).

$$s_L = l \times \sin \theta_1^i \tag{16}$$

where l is the horizontal length of the leg (related to the extent of rotation of the knee joint), and can be obtained by Equation (17).

$$l = l_2 + \Delta l = l_2 + R \sin(\theta_2^i + \alpha) \tag{17}$$

where, R is the distance from the knee joint to the toe, and α is the leg angle ($\alpha = 18.43^\circ$ in Figure 11).

The stride frequency depends on the rotation rate of the servo (w_s); this was $0.18 \text{ s}/60^\circ$ at 7.4 V . A short time Δt elapses between the support and the transfer phase of the leg, maintaining stability. Therefore, the stride frequency is as Equation (18).

$$f = \frac{1}{2\theta_1^i w_s + \Delta t} \tag{18}$$

Finally, the velocity is given by Equation (19).

$$v = \frac{[l_2 + R \sin(\theta_2^i + \alpha)] \sin \theta_1^i}{2\theta_1^i w_s + \Delta t} \tag{19}$$

From Equation (19), as the angle θ_2^i increases, the velocity increases when $\theta_2^i + \alpha < 90^\circ$. When θ_2^i is 37.97° , the leg length is maximal (up to 52.68 mm). Then, the stride length depends only on the angle θ_1^i . To maximize velocity, we sought to define the optimal angle θ_1^i of the horizontal servo.

As the rotatory range of the servo is $0\text{--}90^\circ$, we evaluated nine angles ($10, 20, 30, 40, 50, 60, 70, 80$, and 90°). In Figure 13, the green curve represents the simulated results; the maximum velocity was about 12.0 cm/s when the rotary angle was less than 50° . The deep-sky-blue asterisks indicate the experimental results; the red curve fits these results. The maximum simulated and experimental velocities differed, perhaps because of slipping between the toe and the ground. However, the trends of the two curves were similar. Servo wear was more severe at higher frequencies. We set the optimal angle θ_1^i to 55° .

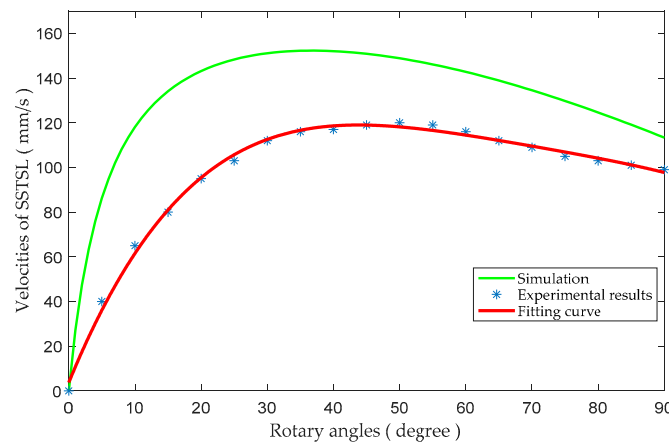


Figure 13. The velocities at different rotary angles of the horizontal servos.

The other parameter affecting velocity is the stride frequency. Ideally, the higher the frequency, the greater the velocity. However, stride frequency cannot be infinite, and slipping will develop at higher frequencies. To evaluate the sliding gaits, we measured velocities when the horizontal servo (set to 55°) operated at various frequencies. On smooth flat terrain, we tested three gaits (i.e., a synchronous gait using two legs, a trot, and a tripod walk). Given the limited performance of the servo, the frequencies of the synchronous sliding gait with two legs (SSGTL) and the trotting walking gait (TTWG) ranged from $0\text{--}2.5 \text{ Hz}$, and that of the tripod walking gait (TPWG) from $0\text{--}1.7 \text{ Hz}$. Figure 14 shows the velocities at different frequencies on smooth flat terrain. With the SSGTL and TPWG, as the gait frequency increased, the velocity initially increased linearly at low frequencies and then declined at high frequencies. For the TTWG, at relatively low frequencies (under 0.5 Hz), the robot could not maintain balance. The robot had only two legs on the ground, so the pressure associated with TTWG was larger than that associated with other gaits, so the velocity slowly declined. With the TPWG (a

four-beat gait), the velocity was lower than those of the other gaits, not exceeding 5.2 cm/s. For SSGTL, the maximum velocity of 16.7 cm/s on smooth flat terrain was attained at 1.5 Hz and increased 13.6% than TTWG.

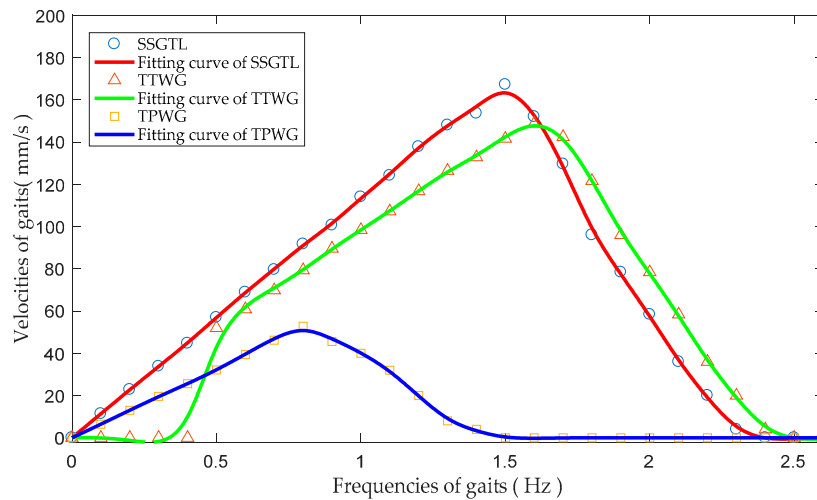


Figure 14. The velocities of gaits with different frequencies on smooth flat terrain. The deep-sky-blue circles, the coral triangles and the orange squares indicate the experimental synchronous sliding gait with two legs (SSGTL), TTWG, and TPWG data. The red, green and blue curves are the fitting curves for these data, respectively.

Figure 15a,b represent the roll, pitch, yaw angle of SSGTL and TTWG, respectively. For both gaits, the roll and pitch angle change slightly while moving. ASR-III with TTWG always swung around the z axes and the swing angle was about 5.1° , and the robot with SSGTL had a slight offset (2.2°). Consequently, compared to the walking gaits, the sliding gait for ASR-III on smooth flat terrain was better in terms of stability.

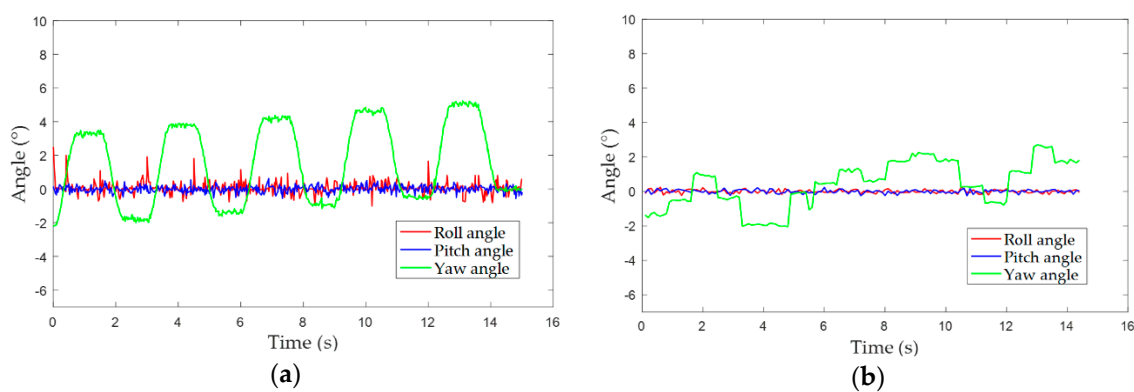


Figure 15. Roll, pitch, yaw angle of WWTG and SSTGL. (a) WWTG; (b) SSTGL.

Figure 16 shows the velocities of TTWG and TPWG on rough terrain (an earth road) at different frequencies. Such terrain is characterized by variations in the friction coefficient and roughness. With increasing frequency, the velocity increased linearly and then fell to zero. For both TTWG and TTPG, the velocity on rough terrain was greater than on smooth flat terrain, attaining 18.5 cm/s at 1.9 Hz and 7.0 cm/s at 1.1 Hz, and increased 20.5% and 28.6%, respectively. Besides, the mean power with SSGTL and TTWG measured approximately at the maximum velocity were 40.5 W and 56.7 W, respectively. According to the customary, we set the output factor of batteries as 80%. The robot can work 3h in the on-land range of the radius of 2.0 km.

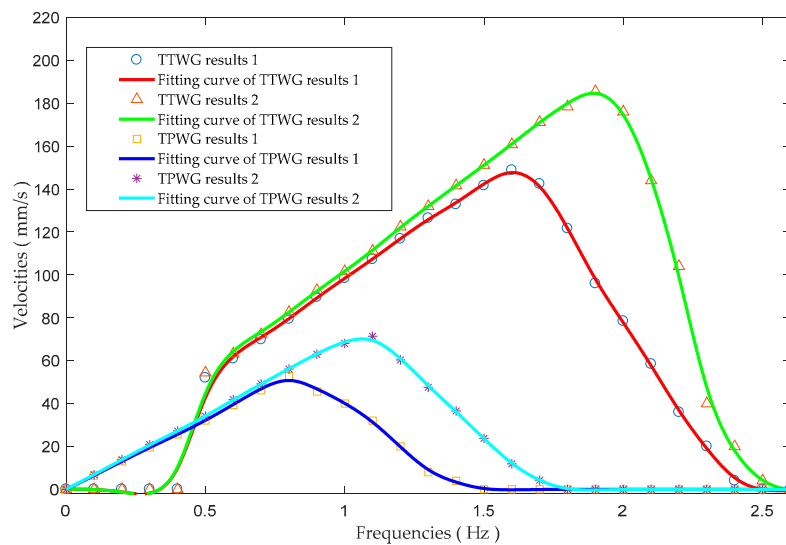


Figure 16. The velocities of gaits of different frequency on smooth flat, and rough, substrates. The deep-sky-blue circles and the coral triangles indicate the experimental TTWG data on smooth, flat and rough terrain, and the orange squares and the purple asterisks indicate the experimental TPWG data on smooth, flat and rough terrains. The red, green, blue and cyan curves are the corresponding fitting curves.

We evaluated rotatory motion using the sliding rotatory gait (SRG) and walking rotatory gait (WRG). In Figure 17, the red and blue curves show the rotatory velocities of the SRG and WRG at different frequencies, respectively. For both rotatory gaits, the rotatory angle of a single step was 90° and the rotatory velocity increased linearly with increasing frequency, to attain a maximum. As the frequency increased further, the rotatory velocity declined rapidly because of slipping. Compared to the WRG, the SRG had a higher rotatory velocity.

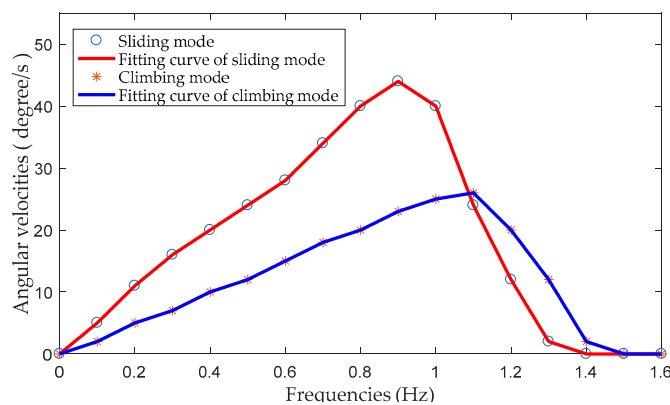


Figure 17. Angular velocity of rotatory movement of the robot on different frequency.

4.4. A Waypoint Tracking Experiment Featuring Closed-Loop Proportional-Integral-Derivative (PID) Control

When an intelligent and multi-functional robot performs real work, a selection of gaits affording excellent performance is essential, as is the ability to track waypoints flexibly and autonomously. A real-time vision localization system is required. Thus, we defined three coordinate systems: a pixel system $\{O^{pixel}\}$, an image system $\{O^i\}$, and a world system $\{O^p\}$. To optimize performance, the optical center axis of the camera lay perpendicular to the object plane. As shown in Figure 18, the robot positions detected by the global camera running the Kalman Consensus Filter (KCF) algorithm

in the image and object planes are (x_r^i, y_r^i) and (x_r^p, y_r^p) respectively. Using the principle of pinhole imaging, we obtain Equations (20) and (21).

$$\begin{bmatrix} x_r^i \\ y_r^i \\ 1 \end{bmatrix} = \begin{bmatrix} \frac{1}{d_x} & 0 & x_0^{pixel} \\ 0 & -\frac{1}{d_y} & y_0^{pixel} \\ 0 & 0 & 1 \end{bmatrix} \begin{bmatrix} x^{pixel} \\ y^{pixel} \\ 1 \end{bmatrix} \tag{20}$$

$$d \begin{bmatrix} x^{pixel} \\ y^{pixel} \\ 1 \end{bmatrix} = \begin{bmatrix} f & 0 & 0 & 0 \\ 0 & f & 0 & 0 \\ 0 & 0 & 1 & 0 \end{bmatrix} \begin{bmatrix} x_r^p \\ y_r^p \\ d \\ 1 \end{bmatrix} \tag{21}$$

Thus, the position of the robot in the experimental scenario is yielded by Equation (22).

$$\begin{cases} x_r^p = \frac{d(x_r^i - x_0^{pixel})d_x}{f} = \frac{d(x_r^i - x_0^{pixel})}{f_x} \\ y_r^p = -\frac{d(y_r^i - y_0^{pixel})d_y}{f} = -\frac{d(y_r^i - y_0^{pixel})}{f_y} \end{cases} \tag{22}$$

where $(x_0^{pixel}, y_0^{pixel})$ are the principal point coordinates relative to the image plane, and f_x and f_y are the focal lengths of the camera in the x and y directions, respectively.

We established four waypoints (A, B, C, and D; the corners of a rectangle). Figure 19 shows the experimental scenario that the ASR-III is on the blue ground. The camera software calculates the position of the robot using Equation (22) and sends the information to the robot. As described in Appendix A, we designed a waypoint tracking algorithm featuring precise positional and heading angle control, and allowed flexible locomotion (as described above). In waypoints tracking algorithm (Algorithm A1 in Appendix A), the parameter δ_d is the distance threshold; when the distance from the current position to the next waypoint is less than δ_d , we consider that the robot has arrived at the waypoint.

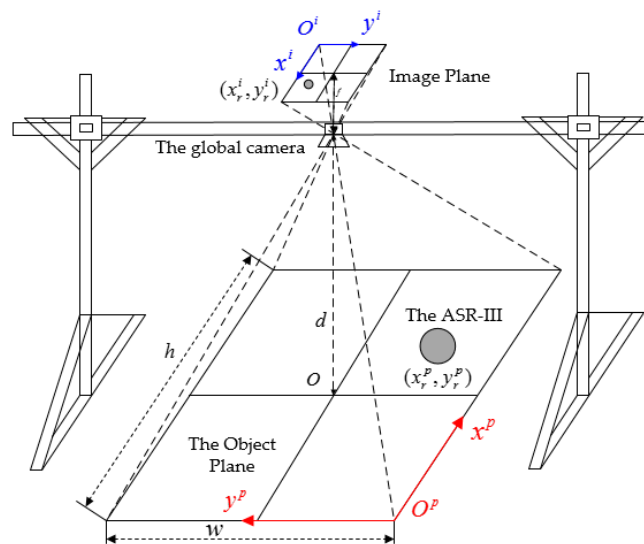


Figure 18. The vision localization system and the global camera. The gray circle indicates the ASR-III.

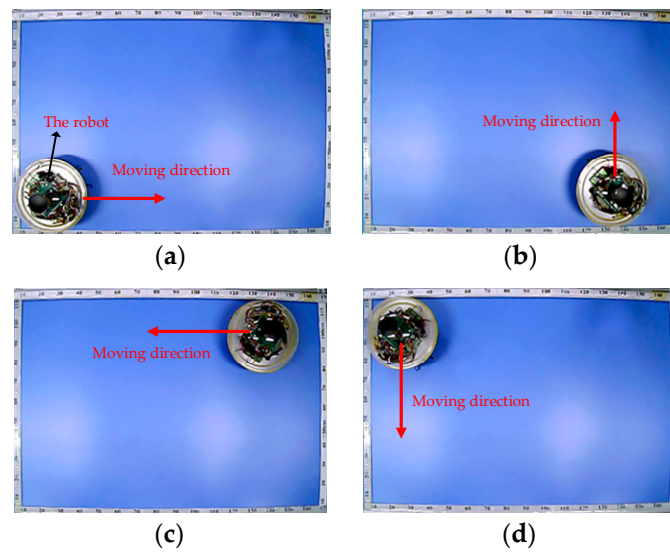


Figure 19. Snapshots of waypoint tracking (view of the global camera). (a) at point A; (b) at point B; (c) at point C; (d) at point D.

A common steering method used for legged robots on both sides is known as differential drive, where the swing angle α_{robot} is proportional to the difference between left α_l and right α_r leg angles. In the heading angle control algorithm (Algorithm A2 in Appendix A), we implemented a closed loop PID controller that ran at 50 Hz and an open loop controller. In the closed loop PID controller, IMU (JY901 IMU module) readings of yaw angle provided feedback, and the PID controller monitors proportional, integral, and derivative errors in order to output the PWM values required for achieving the desired swing angles of legs. As described in Algorithm A2 in Appendix A, when orientation errors appear, the robot need to adjust it direction by swing angles of both sides of legs. The parameter δ_a is an angle threshold; when the orientation error is less than δ_a , the robot goes forward with different swing angles of legs. When the orientation error is larger than δ_a , the robot stops to rotate with the rotary gait, and goes forward only until the orientation decline under δ_a . In the open loop controller, the difference of left legs and right legs was calculated by the distance from the current position to the reference trajectory. The longer the distance, the larger the difference.

The waypoint tracking experiment is shown in Figure 19, as captured by the global camera at A, B, C, and D. In Figure 20, the four red stars are the four waypoints, and the blue lines are the reference trajectory. The vision localization system of the global camera records the trajectory (black curves) when the parameters δ_d and δ_a are 3 cm and 8° , respectively. With the experiment's data of ASR-III trajectory, the maximum offsets with closed-loop PID and an open loop PID were about 7.0 cm and 10 cm, and the mean offset were up to 3.42 cm and 4.16 cm. Compared to the open loop trajectory, the maximum and mean offset with closed-loop PID reduced 30% and 17.9%, respectively. In order to evaluate the performance of the waypoints tracking with closed-loop PID, we also recorded the heading angle as shown in Figure 21. The maximum offsets with closed-loop PID and open loop manner were 8.6° and 10.4° . The mean offset with closed-loop PID and open loop manner were about 1.86° and 4.15° . Compared to the heading angle with open loop manner, the maximum and mean offset with closed-loop PID reduced 17.3% and 55.2%. In addition to the imperfect motion caused by the manufacturing tolerance, the robot location obtained by the vision localization system also had a slightly error because of the variations in illumination. However, compared to the size (35 cm) of the robot, the maximum trajectory offset with closed-loop PID only occupied 1/5, which was really slight offset. The heading angle exhibited several fluctuations, but the robot effectively corrected them. As a result, apart from several slight drifts, the robot tracked the task with less great precision, guided by the vision localization system.

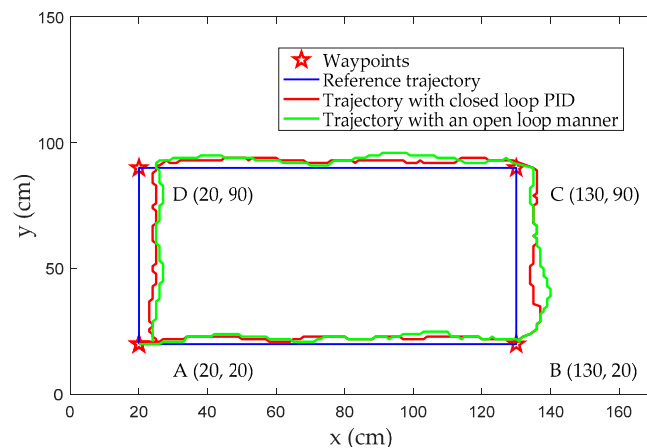


Figure 20. The experimental waypoint trajectory. The red stars represent the waypoints. We show the four waypoints A (20, 20), B (130, 20), C (130, 90), and D (20, 90), and the reference trajectory (blue lines; a precise rectangle). The red and green curves are the trajectory of the robot with closed loop PID and an open loop manner as recorded by the vision localization system, respectively.

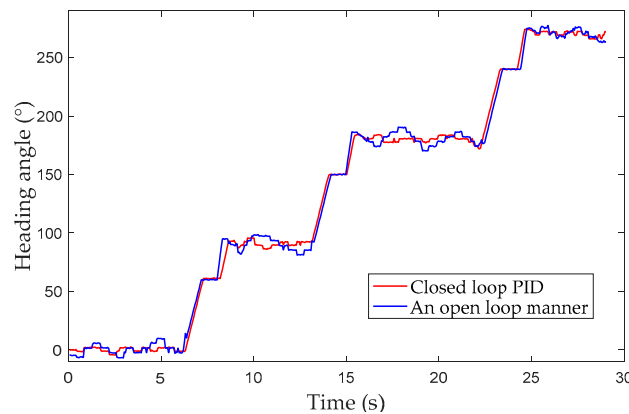


Figure 21. The heading angle in waypoint trajectory experiment. The red and blue curves represent heading angle with closed loop PID and an open loop manner, respectively.

5. The Underwater Locomotion Experiments

Due to the symmetrical spherical design, the robot has the same model for forward motion and backward motion. Hence experiments in forward motion were carried out to evaluate the performance of ASR-III underwater motions. Figure 22 shows the video sequence of the forward motion of ASR-III on the water surface of the pool with the size of 3 m × 2 m × 1 m (height × width × depth). In the pool, there were two vertical rulers (2 m) and one horizontal ruler (2.5 m). We assumed that the water was static. As depicted in Section 3, we adapted the forward motion strategy with four thrusters. The motor of thruster worked under the voltage of 20 V. Initially the robot was put at one side of the horizontal ruler, and then swam along the ruler to other side. We recorded the time and the displacement of forward motion, and then calculate the velocity. As shown in Figure 23, the red and blue curves indicate the displacement and the velocity of the robot varying with time. The robot speeded up to the maximum velocity (21.5 cm/s, 0.61 body/s) at about 6.5 s, and then the robot swam at the constant speed. From the start to the end, the average velocity of the robot was 18.1 cm/s (0.52 body/s). Furthermore, the mean power measured approximately at maximum velocity was 64.5 W, and the robot can cruise 2.5 h in the range of the radius of 1.5 km.

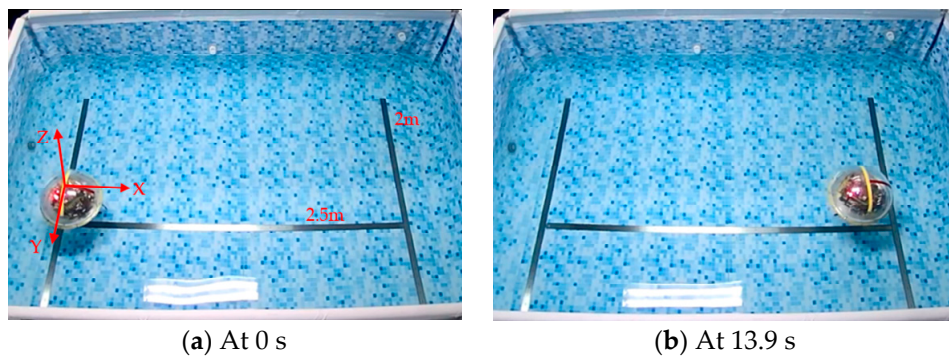


Figure 22. Underwater forward motion on the water surface.

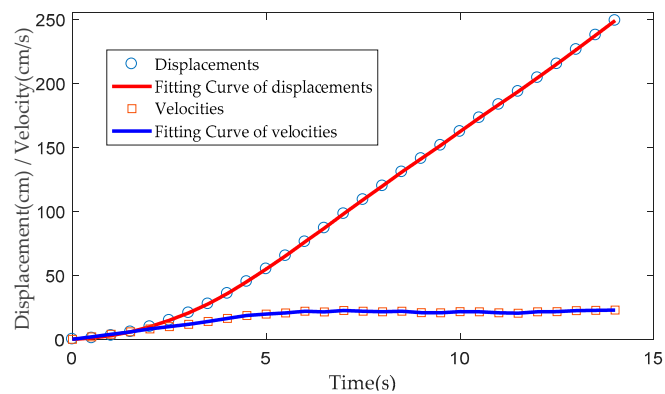


Figure 23. Experimental results for forward motion.

The heading angle control experiment was conducted to evaluate the performance of ASR-III with the strategy of the left turning and right turning. The heading angle measured by the JY901 IMU module was regarded as the feedback for the closed-loop control. The experiment was carried out in the same pool. Figure 24 shows four snapshots of the heading angle control motion. The initial angle of the robot was set to 0° , and the expected heading angle was set to 90° . As shown in Figure 25a, the robot can keep stable at 16.5 s.

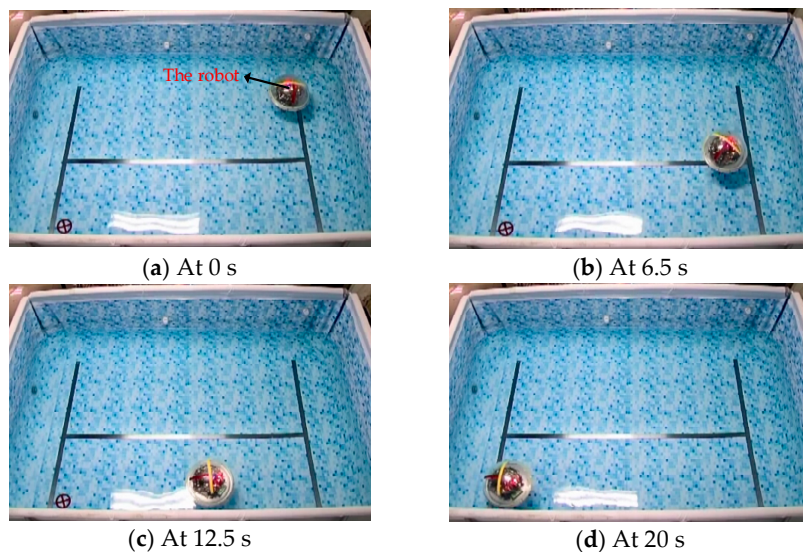


Figure 24. Heading angle control underwater motion on the water surface.

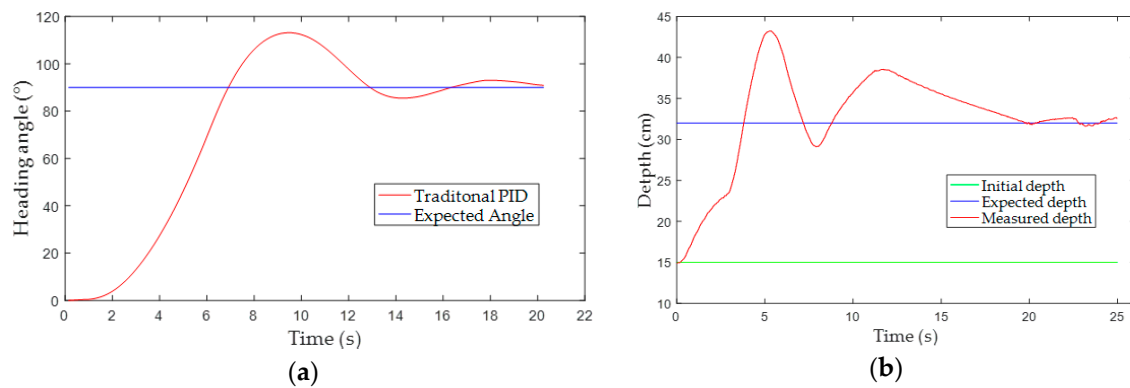


Figure 25. (a) Experimental results for heading angle control; (b) experimental results for depth control.

Besides the forward motion and the heading angle control experiment, the depth control experiment was carried out to evaluate the performance of ASR-III with the strategy of floating and sinking. The depth values were collected by IIC bus from the pressure sensor (MS5803-01BA module) installed under the middle plant, and regarded as the feedback for the closed-loop PID control. The robot started at a depth of 15 cm, and the expected depth was 32 cm. The results of depth control were illustrated in Figure 25b. The robot reached the expected depth after 20 s. In the steady state, the mean depth error was 0.56 cm.

6. Discussion

Based on the results obtained from the experiments, on land locomotion and underwater locomotion were concluded. First, the LSWM was evaluated to make the robot stand up and slide on smooth flat ground. We obtained the relationship between the rising and falling velocity v and the duty factor s , which assisted the robot realizing the automatic lifting and dropping of the LSWM. Second, the two parameters which affected the velocity of the robot on land were the stride length and frequency. After experiments, we found that the optimal rotary angle was 55° . On smooth flat terrain, the maximum velocity of SSTGL (sliding locomotion) was 16.7 cm/s at 1.5 Hz and increased 13.6% than TTWG (walking locomotion), which proved that SSTGL on smooth flat terrain had higher velocity performance than TTWG for ASR-III. On rough terrain, the maximum velocity of TTWG is 18.5 cm/s at 1.9 Hz. In addition, the mean power with SSTGL and TTWG measured approximately at the maximum velocity were 40.5 W and 56.7 W, respectively, which testified the low power loss of SSTGL. Compared to the maximum velocity (8.5 cm/s) of the previous robot [37], the maximum velocity of TTWG was about twice higher. For the rotatory gait, the maximum rotatory velocity in previous robot [38] was up to $67^\circ/s$ while the weight of the robot was only 2.1 KG. However, Now ASR-III's weight was up to 8.2 KG (about four times heavier than the previous robot), and the rotatory velocity was $44.5^\circ/s$ (decline 33.6%). Third, for the waypoints tracking, the maximum trajectory offset with closed-loop PID only occupied 1/5 to the size (35) of the robot, which was really slight offset. Finally, underwater locomotion, such as forward motion, backward motion, turn left or right, floating and sinking were realized. Compared to the previous work [36] in forward locomotion, the average velocity of the robot was just 10 cm/s (0.29 body/s), and increased about 81%. For the heading angle control, the robot can keep the expected angle at 25 s, and the time was shortened about 34% compared to the previous work [36]. For the depth control, the robot has a sensitive response, and the control errors are in the acceptable range. Besides, with the comparison to the related works, Locomotion speed of ASR-III on ground was slower than AmphiBot II [12], and locomotion speed of ASR-III in water was almost equal to AmphiBot II. However, the robot can rotate with zero-radius both on land and in water, and have a stable heading angle control. Compared to the hexapedal robot [16], ASR-III on ground and in water was slower than the hexapedal robot. However, our robot can realize

multi-locomotion, such as sinking down and floating up in water, rotating with zero-radius both on land and in water. In addition, the robot can keep a stable depth in water for some complex tasks.

7. Conclusions

We describe the novel, multiply gaited, vectored water-jet hybrid locomotion-capable, amphibious, spherical robot III. To improve on-land velocity on different substrates and decrease the payload on the leg servos, we designed an automated lifting and supporting mechanism with four omni-directional wheels to facilitate sliding locomotion, and also the transition between smooth flat and rough terrain; two platform servos were synchronously controlled. The efficacy of the LSWM was verified experimentally.

To improve stability and mobility on land, we designed sliding gaits for smooth flat terrain and walking gaits for rough terrain. We experimented with different gaits on different substrates to define the optimal gaits. Compared with walking gaits, sliding locomotion using SSGTL or SRG afforded good stability and mobility on smooth flat terrain, and relatively higher velocities. Walking gaits caused the swing of the robot, which reduces stability. However, TTWG and TPWG can be used on rough terrain, and the speed increased 20.5% and 28.6% than on smooth terrain. The maximum speed is almost double that of the previous work. In terms of rotation, SRG exhibited a higher rotatory velocity (up to $44.5^\circ/\text{s}$) than WRG. Although the weight of the robot increased almost four times, the robot also rotates smoothly with a high angular velocity. In addition, we developed a waypoint tracking algorithm combining a vision localization system with a global camera. The maximum offset of this trajectory is just $1/5$ of the diameter of the robot, which showed experimentally that the robot performed well.

The robot can also realize the underwater locomotion with four vectored water-jet thrusters. Compared to the previous work, the maximum velocity of forward motion increased 81%, and the time to be stable in heading angle control was shortened 34%. Besides, the robot also has a sensitive response in depth control, and the control errors are in the acceptable range. Therefore, the performance of underwater locomotion was improved.

With the high performance of the robot in amphibious environment, we will build multiple robot system in future.

Acknowledgments: This work was supported by National Natural Science Foundation of China (61503028, 61773064, 61375094), and Excellent Young Scholars Research Fund of Beijing Institute of Technology (2014YG1611). This research project was also partly supported by National High Tech. Research and Development Program of China (No. 2015AA043202).

Author Contributions: Huiming Xing conceived and designed the experiments, and then wrote the paper; Shuxiang Guo and Liwei Shi guided the system design and revised the manuscript. Yanlin He, Shuxiang Su and Zhan Chen performed the experiments. Xihuan Hou analyzed the data.

Conflicts of Interest: The authors declare no conflict of interest.

Appendix A. Waypoints Tracking Algorithm

As mentioned in Section 5, we designed a waypoint tracking algorithm including position and heading angle control. The following three algorithms are the position control algorithm, the heading angle control algorithm, and the waypoint tracking algorithm, respectively.

Algorithm A1 Waypoints tracking algorithm with Closed-loop PID Control

- 1: **System Initialization**
 - 2: **Waypoints set up**
 - 3: **Go to the next waypoint** (w_x^i, w_y^i)
 - 4: Calculate the distance $d = \sqrt{(w_x^i - x_r)^2 + (w_y^i - y_r)^2}$
 - 5: **IF** $d < \delta_d$
 - 6: **IF** this waypoint is the last one
 - 7: Waypoints tracking ends
 - 8: **ELSE**
 - 9: Go to the next waypoint
 - 10: **ELSE**
 - 11: **IF** Road is smooth
 - 12: Do ASR-III sliding motion with heading angle control
 - 13: **ELSE**
 - 14: Do ASR-III climbing motion with heading angle control
-

Algorithm A2 Heading Angle control algorithm

- 1: Initial the parameters
 - 2: Read the current heading angle
 - 3: Calculate the differential angle $\alpha = \alpha_{expected} - \alpha_{heading}$
 - 4: **While**
 - 5: **IF** $\alpha \geq \delta_a$ or $\alpha \leq -\delta_a$
 - 6: Get Leg PID angle α_p
 - 7: Swing angle of legs $\alpha_{legs} \leftarrow \alpha_i + \alpha_p$
 - 8: Stop and execute the sliding rotary gait
 - 9: **ELSE**
 - 10: Get leg PID angle α_p
 - 11: **IF** $0 < \alpha < \delta_a$ (turn left)
 - 12: Left legs $\alpha_l \leftarrow \alpha_i - \alpha_p$
 - 13: Right legs $\alpha_r \leftarrow \alpha_i + \alpha_p$
 - 14: **ELSE**
 - 15: Left legs $\alpha_l \leftarrow \alpha_i + \alpha_p$
 - 16: Right legs $\alpha_r \leftarrow \alpha_i - \alpha_p$
 - 17: Go forward with different swing angles
 - 18: **End while**
-

References

1. Shi, Q.; Li, C.; Wang, C.B.; Luo, H.B.; Huang, Q.; Fukuda, T. Design and Implementation of an Omnidirectional Vision System for Robot Perception. *Mechatronics* **2017**, *41*, 58–66. [[CrossRef](#)]
2. He, Y.L.; Guo, S.X.; Shi, L.W. Preliminary Mechanical Analysis of an Improved Amphibious Spherical Father Robot. *Microsyst. Technol.* **2016**, *22*, 2051–2066. [[CrossRef](#)]
3. Guo, S.X.; Pan, S.W.; Li, X.Q.; Shi, L.W. A System on Chip-based Real-time Tracking System for Amphibious Spherical Robots. *Int. J. Adv. Robot. Syst.* **2017**, *14*, 1–19. [[CrossRef](#)]
4. Guo, S.X.; Pan, S.W.; Shi, L.W. Visual Detection and Tracking System for an Amphibious Spherical Robot. *Sensors* **2017**, *17*, 870. [[CrossRef](#)] [[PubMed](#)]
5. Kaznov, V.; Seeman, M. Outdoor Navigation with a Spherical Amphibious Robot. In Proceedings of the IEEE/RSJ International Conference on Intelligent Robots and Systems, Taipei, Taiwan, 18–22 October 2010.
6. Shi, Q.; Ishii, H.; Sugahara, Y.; Sugita, H.; Takanishi, A.; Huang, Q.; Fukuda, T. Design and Control of a Biomimetic Robotic Rat for Interaction with Laboratory Rats. *IEEE/ASME Trans. Mechatron.* **2015**, *20*, 1832–1842. [[CrossRef](#)]

7. Shi, Q.; Ishii, H.; Kinoshita, S.; Konno, S.; Takamishi, A.; Okabayashi, S.; Iida, N.; Kimura, H.; Shibata, S. Modulation of Rat Behaviour by Using a Rat-like Robot. *Bioinspir. Biomim.* **2013**, *8*, 046002. [[CrossRef](#)] [[PubMed](#)]
8. Shi, Q.; Ishii, H.; Tanaka, K.; Sugahara, Y.; Takamishi, A.; Okabayashi, S.; Huang, Q.; Fukuda, T. Behavior Modulation of Rats to a Robotic Rat in Multi-rat Interaction. *Bioinspir. Biomim.* **2015**, *10*, 050611. [[CrossRef](#)] [[PubMed](#)]
9. Jun, B.H.; Shim, H.; Kim, B.; Park, J.Y.; Baek, H.; Lee, P.M.; Kim, W.J.; Park, Y.S. Preliminary Design of the Multi-Legged Underwater Walking Robot CR200. In Proceedings of the Oceans MTS/IEEE Conference, Yeosu, Korea, 21–24 May 2012.
10. Shim, H.; Yoo, S.Y.; Kang, H.; Jun, B.H. Development of Arm and Leg for Seabed Walking Robot CRABSTER200. *Ocean Eng.* **2016**, *116*, 55–67. [[CrossRef](#)]
11. Crespi, A.; Karakasiotis, K.; Guignard, A.; Ijspeert, A.J. Salamandra Robotica II: An Amphibious Robot to Study Salamander-Like Swimming and Walking Gaits. *IEEE Trans. Robot.* **2013**, *29*, 308–320. [[CrossRef](#)]
12. Crespi, A.; Ijspeert, A.J. AmphiBot II: An Amphibious Snake Robot that Crawls and Swims using a Central Pattern Generator. *Color Res. Appl.* **2006**, *27*, 130–135.
13. Tang, Y.G.; Zhang, A.Q.; Yu, J.C. Modeling and Optimization of Wheel-Propeller-Leg Integrated Driving Mechanism for an Amphibious Robot. In Proceedings of the 2nd International Conference on Information and Computing Science, Manchester, UK, 21–22 May 2009; pp. 73–76.
14. Zhang, S.W.; Zhou, Y.C.; Xu, M.; Liang, X.; Liu, L.; Yang, J. AmphiHex-I: Locomotory Performance in Amphibious Environments with Specially Designed Transformable Flipper Legs. *IEEE-ASME Trans. Mechatron.* **2016**, *21*, 1720–1731. [[CrossRef](#)]
15. Sun, Y. Planning of Legged Racewalking Gait for an Epaddle-Based Amphibious Robot. *IFAC Proc. Vol.* **2012**, *45*, 218–223. [[CrossRef](#)]
16. Kim, H.; Lee, D.; Liu, Y.; Seo, T.; Jeong, K. Hexapedal Robot for Amphibious Locomotion on Ground and Water. In Proceedings of the IEEE/ASME International Conference on Advanced Intelligent Mechatronics (AIM), Busan, Korea, 7–11 July 2015; pp. 121–126.
17. Aoki, T.; Ito, S.; Sei, Y. Development of quadruped walking robot with spherical shell-mechanical design for rotational locomotion. In Proceedings of the IEEE/RSJ International Conference on Intelligent Robots and Systems, Hamburg, Germany, 28 September–2 October 2015; pp. 5706–5711.
18. Yin, X.; Wang, C.; Xie, G. A salamander-like amphibious robot: System and control design. In Proceedings of the International Conference on Mechatronics and Automation, Chengdu, China, 5–8 August 2012; pp. 956–961.
19. Boxerbaum, A.S.; Werk, P.; Quinn, R.D.; Vaidyanathan, R. Design of an Autonomous Amphibious Robot for Surf Zone Operation: Part I Mechanical Design for Multi-Mode Mobility. In Proceedings of the IEEE/ASME International Conference on Advanced Intelligent Mechatronics, Monterey, CA, USA, 24–28 July 2005; pp. 1459–1464.
20. Harkins, R.; Ward, J.; Vaidyanathan, R.; Boxerbaum, A.S.; Quinn, R.D. Design of an Autonomous Amphibious Robot for Surf Zone Operations: Part II—Hardware, Control Implementation and Simulation. In Proceedings of the IEEE/ASME International Conference on Advanced Intelligent Mechatronics, Monterey, CA, USA, 4–28 July 2005; pp. 1465–1470.
21. Li, B.; Ma, S.G.; Ye, C.L.; Yu, S.M.; Zhang, G.W.; Gong, H.L. Development of an Amphibious Snake-like Robot. In Proceedings of the 8th World Congress on Intelligent Control and Automation (WCICA), Jinan, China, 6–9 July 2010; pp. 613–618.
22. Hirose, S.; Yamada, H. Snake-like Robots: Machine Design of Biologically Inspired Robots. *IEEE Robot. Autom. Mag.* **2003**, *16*, 88–98. [[CrossRef](#)]
23. Pan, S.W.; Guo, S.X.; Shi, L.W.; He, Y.L.; Wang, Z.; Huang, Q. A Spherical Robot based on all Programmable SoC and 3-D Printing. In Proceedings of the 11th IEEE International Conference on Mechatronics and Automation (ICMA), Tianjin, China, 3–6 August 2014; pp. 150–155.
24. He, Y.L.; Guo, S.X.; Shi, L.W.; Pan, S.W.; Wang, Z. 3D Printing Technology-based an Amphibious Spherical Robot. In Proceedings of the 11th IEEE International Conference on Mechatronics and Automation (ICMA), Tianjin, China, 3–6 August 2014; pp. 1382–1387.

25. He, Y.L.; Shi, L.W.; Guo, S.X.; Guo, P.; Xiao, R. Numerical Simulation and Hydrodynamic Analysis of an Amphibious Spherical Robot. In Proceedings of the IEEE International Conference on Mechatronics & Automation, Beijing, China, 2–5 August 2015; pp. 848–853.
26. Pan, S.W.; Shi, L.W.; Guo, S.X.; Guo, P.; He, Y.L.; Xiao, R. A Low-power SoC-based Moving Target Detection System for Amphibious Spherical Robots. In Proceedings of the IEEE International Conference on Mechatronics & Automation, Beijing, China, 2–5 August 2015; pp. 1116–1121.
27. Shi, L.W.; Xiao, R.; Guo, S.X.; Guo, P.; Pan, S.W.; He, Y.L. An Attitude Estimation System for Amphibious Spherical Robots. In Proceedings of the IEEE International Conference on Mechatronics & Automation, Beijing, China, 2–5 August 2015; pp. 2076–2081.
28. Pan, S.W.; Shi, L.W.; Guo, S.X. A Kinect-Based Real-Time Compressive Tracking Prototype System for Amphibious Spherical Robots. *Sensors* **2015**, *15*, 8232–8252. [[CrossRef](#)] [[PubMed](#)]
29. Guo, J.; Guo, S.X.; Li, L.G. Design and Characteristic Evaluation of a Novel Amphibious Spherical Robot. In Proceedings of the 3rd International Conference on Engineering and Technology Innovation (ICETI), Kenting, Taiwan, 31 October–4 November 2014; Volume 23, p. 6.
30. Nishimura, Y.; Mikami, S. Learning Adaptive Escape Behavior for Wheel-Legged Robot by Inner Torque Information. In Proceedings of the 2016 Joint 8th International Conference on Soft Computing and Intelligent Systems (SCIS) and 17th International Symposium on Advanced Intelligent Systems, Sapporo, Japan, 25–28 August 2016; pp. 10–15.
31. Endo, G.; Hirose, S. Study on Roller-Walker (system integration and basic experiments). In Proceedings of the 1999 IEEE International Conference on Robotics and Automation, Detroit, MI, USA, 10–15 May 1999.
32. Endo, G.; Hirose, S. Study on Roller-Walker—Adaptation of characteristics of the propulsion by a leg trajectory. In Proceedings of the IEEE/RSJ International Conference on Intelligent Robots and Systems, Nice, France, 22–26 September 2008; pp. 1532–1537.
33. Endo, G.; Hirose, S. Study on Roller-Walker—Energy efficiency of Roller-Walk. In Proceedings of the 2011 IEEE International Conference on Robotics and Automation, Shanghai, China, 9–13 May 2011; pp. 5050–5055.
34. Endo, G.; Hirose, S. Study on Roller-Walker (multi-mode steering control and self-contained locomotion). In Proceedings of the IEEE International Conference on Robotics and Automation, San Francisco, CA, USA, 24–28 April 2000; Volume 3, pp. 2808–2814.
35. Li, M.X.; Guo, S.X. A Roller-Skating/Walking Mode-based Amphibious Robot. *Robot. Comput. Integr. Manuf.* **2017**, *44*, 17–29. [[CrossRef](#)]
36. Shi, L.W.; Su, S.X.; Guo, S.X. A Fuzzy PID Control Method for the Underwater Spherical Robot. In Proceedings of the IEEE International Conference on Mechatronics & Automation, Takamatsu, Japan, 6–9 August 2017; pp. 626–631.
37. Shi, L.W.; Pan, S.W.; Guo, S.X. Design and Evaluation of Quadruped Gaits for Amphibious Spherical Robots. In Proceedings of the IEEE International Conference on Robotics and Biomimetics, Qingdao, China, 3–7 December 2017; pp. 13–18.
38. Li, M.X.; Guo, S.X. Design and performance evaluation of an amphibious spherical robot. *Robot. Auton. Syst.* **2015**, *64*, 21–34. [[CrossRef](#)]



© 2018 by the authors. Licensee MDPI, Basel, Switzerland. This article is an open access article distributed under the terms and conditions of the Creative Commons Attribution (CC BY) license (<http://creativecommons.org/licenses/by/4.0/>).